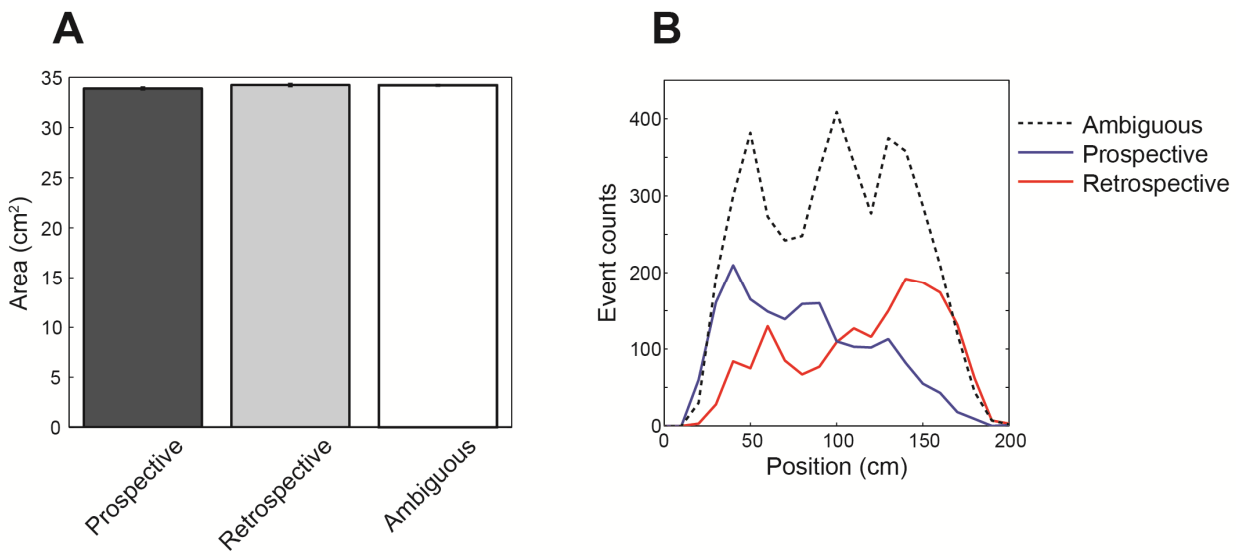

Figure S1, Related to Figure 1. Characterization of prospective and retrospective coding events. (A) Prospective and retrospective coding are not explained by position tracking errors. The area encompassed by LEDs on the headstage used for tracking was determined from raw video files. If prospective coding was due to erroneous position tracking caused by obstruction of the back row of LEDs on the headstage and retrospective coding was due to obstruction of the front row of LEDs on the headstage, then the area measured for the LEDs should have been reduced for retrospective and prospective coding events compared to ambiguous events. However, no difference in the area of the LEDs was observed between prospective, retrospective, and ambiguous events. (B) Prospective and retrospective coding events correlate with different locations on the linear track. Prospective coding events tended to occur as rats were leaving the end of the track. Retrospective coding events tended to occur as rats approached the end of the track. Ambiguous events were observed more often than prospective and retrospective events and occurred on both the ends and the middle of the track.

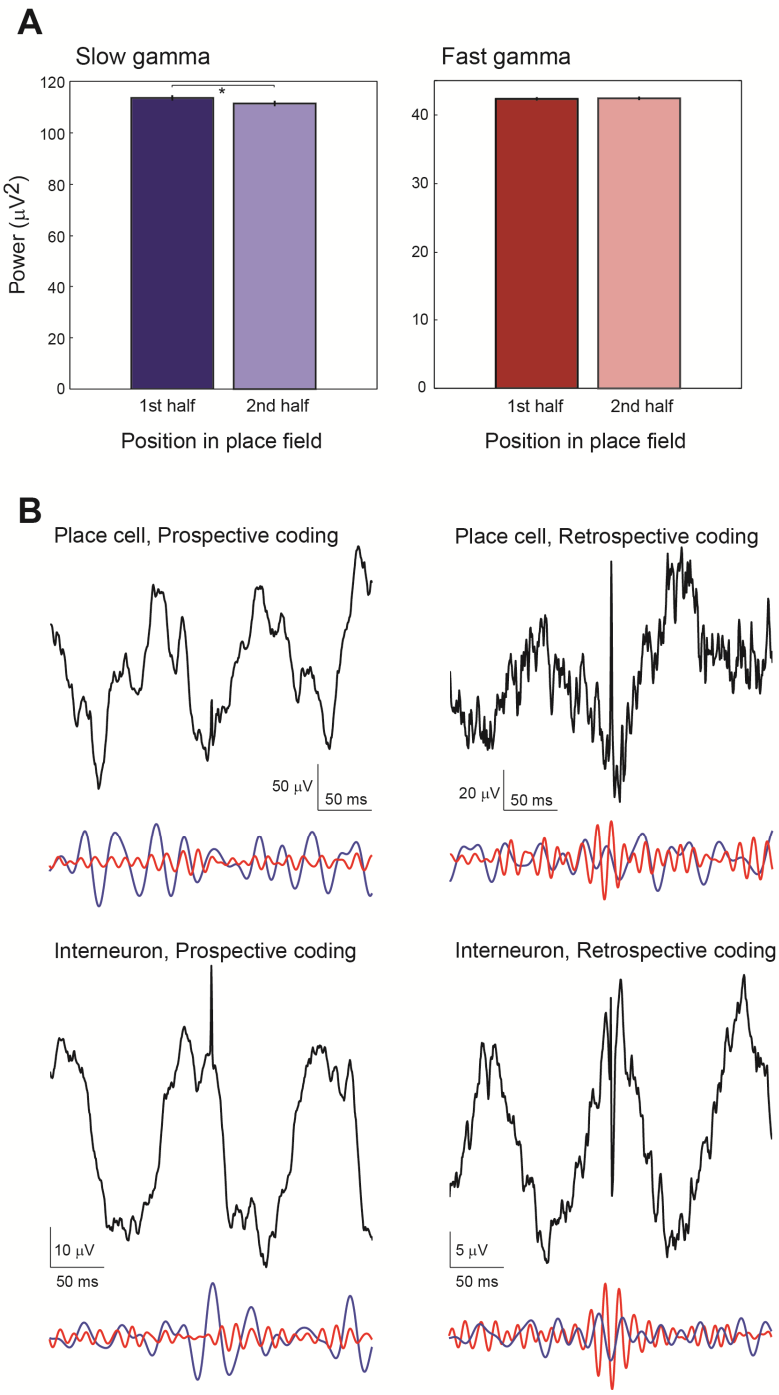

Figure S2, Related to Figure 2. (A) Slow and fast gamma power during the first and second halves of place fields during ambiguous runs. Slow and fast gamma power were measured during the first and second halves of place fields during runs that were classified as ambiguous. Slow gamma power was larger during the first half of place

fields compared to the second half. No difference in fast gamma power was observed between the early and late portions of place fields. (B) Spike triggered averages (STAs) of LFP recordings for example place cells and interneurons during periods of prospective and retrospective coding. For each example, raw traces are shown above, and bandpass filtered versions are shown below (blue: 25-55 Hz, red: 60-100 Hz). Note how robust slow gamma rhythms can be seen in the STAs during prospective coding, and fast gamma rhythms can be seen in the STAs during retrospective coding.

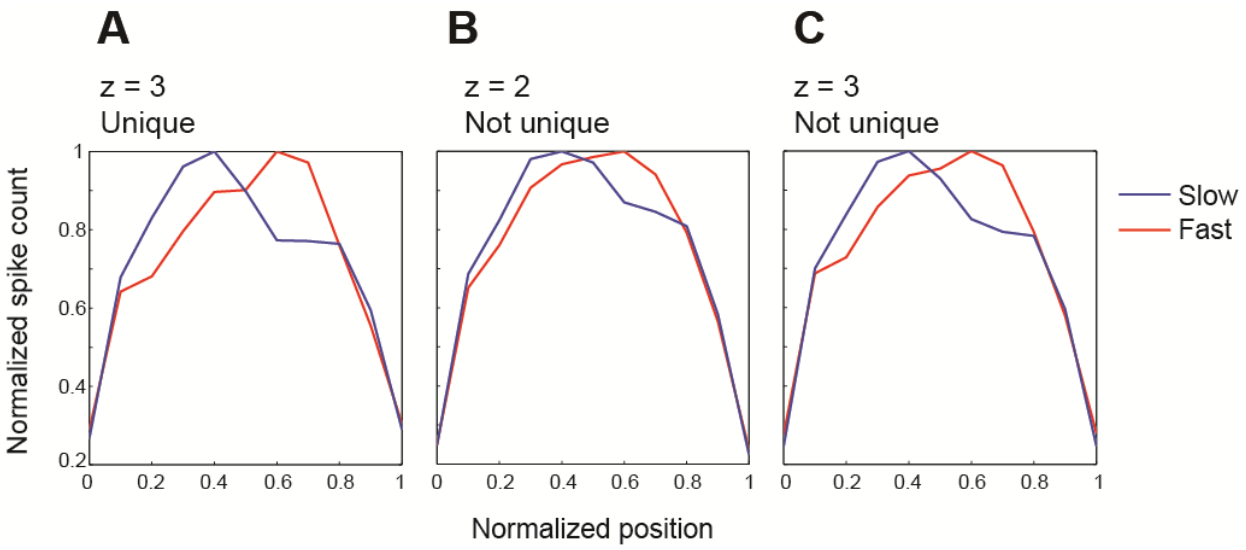

Figure S3, Related to Figure 3. Place fields constructed from spikes during slow and fast gamma periods in CA1 detected using various criteria. (A) Normalized spike counts across position constructed for all spikes from all cells, for spikes subsampled from non-overlapping slow and fast gamma periods detected using a threshold of 3 SD above the mean slow and fast gamma power. (B, C) Normalized spike counts across position for spikes during all slow and fast gamma periods (i.e., including those periods when both slow and fast gamma power exceeded the threshold). Slow and fast gamma were detected by identifying periods when slow and fast gamma power exceeded thresholds of 2 (B) and 3 (C) SD above the mean slow and fast gamma power. Spike counts and position were normalized, and leftward runs were reversed, as described in Figure 3B.

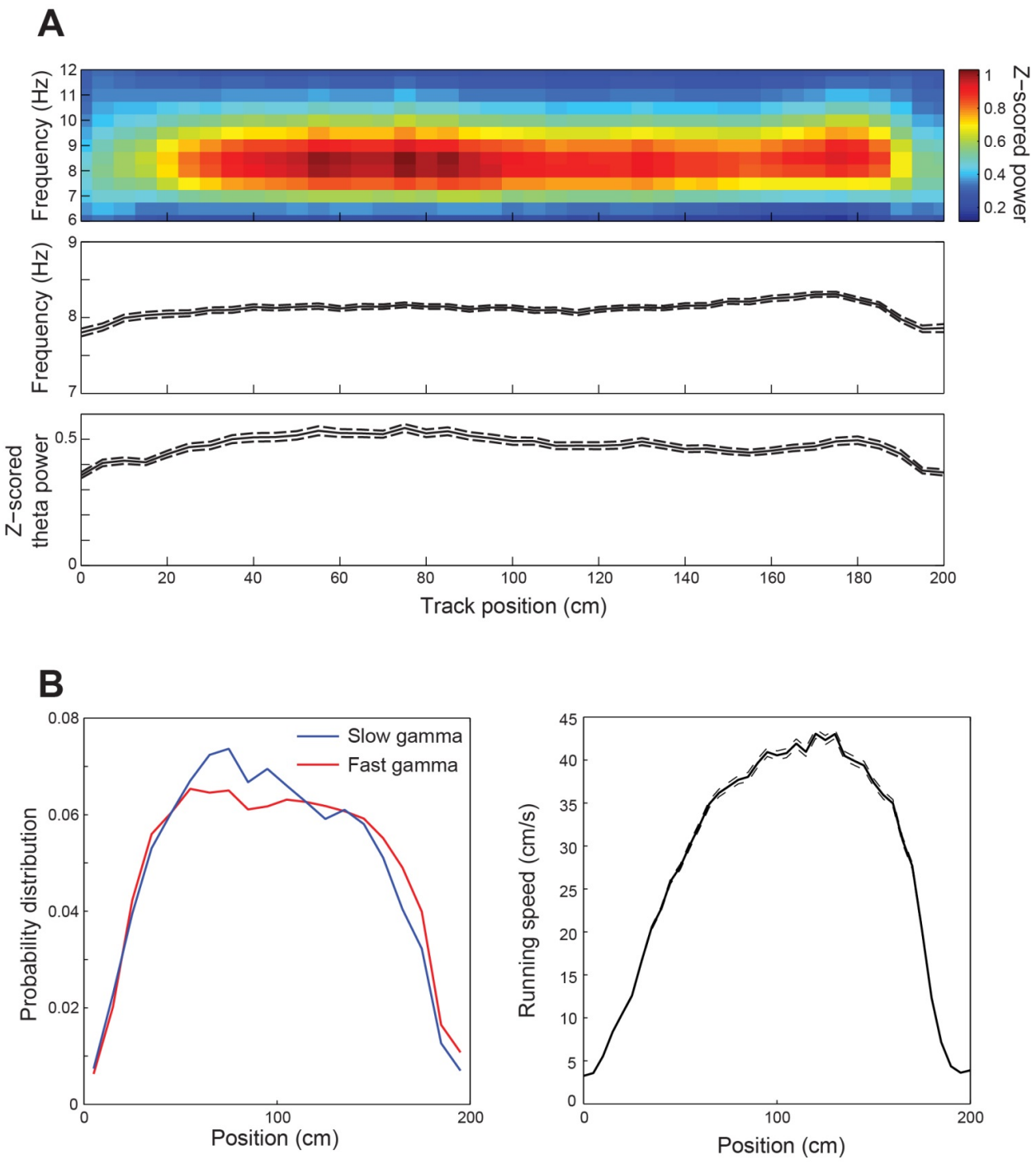

Figure S4, Related to Figure 5. (A) Theta power and frequency at different positions along the linear track. The top panel depicts color-coded power (z-scored) across track position (x-axis) for theta frequencies (y-axis). The middle panel plots the peak frequency of theta (mean ± S.E.M.) across track position. The bottom panel shows z-

scored theta power as a function of track position. Rats were moving in the direction from position = 0 to 200 cm. (B) (Left) The probability of slow and fast gamma occurrence is plotted against position on the linear track. Probabilities were dwell time normalized. Leftward runs were reversed, so that the direction of rat movement is from 0 cm to 200 cm. (Right) Mean running speed (± 95% confidence intervals) is plotted against position on the linear track. Note how locations where slow and fast gamma tended to occur on the linear track cannot be explained by correlations between gamma frequency and running speed (Ahmed and Mehta, 2012).

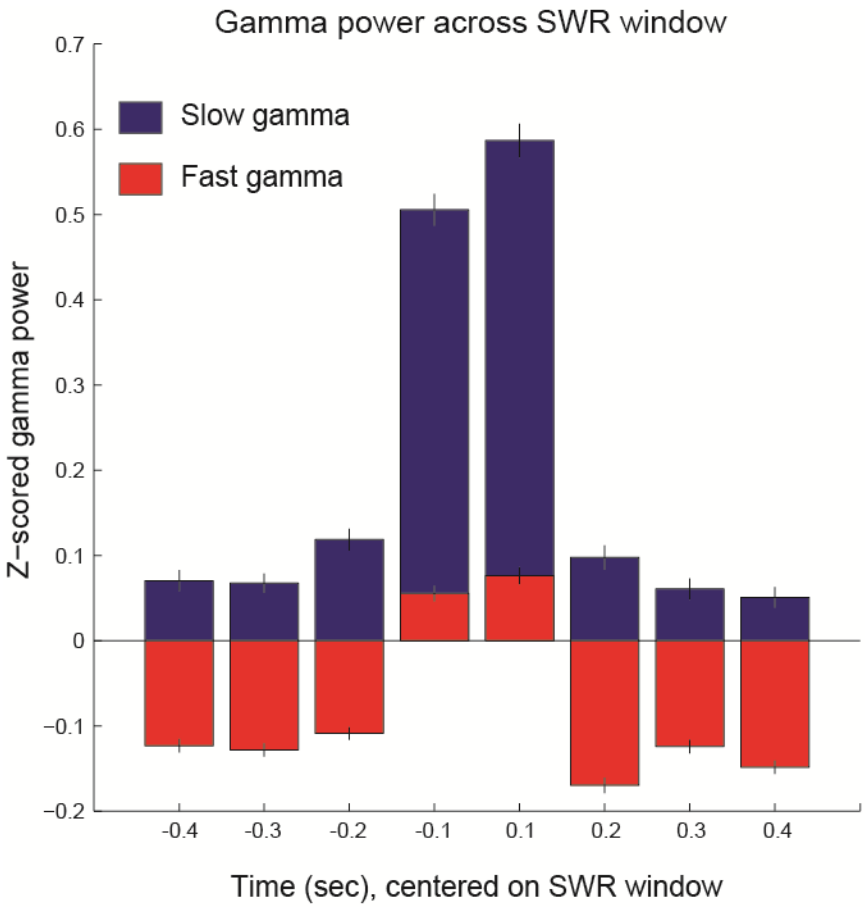

Figure S5, Related to Figure 7. Increase in slow gamma power during sharp wave ripples (SWRs). Time = 0 corresponds to peak ripple power. SWRs were detected as described in Carr et al. (2012). Both slow and fast gamma power increased during SWRs, but slow gamma power increased significantly more than fast gamma power ($F(1,4964) = 194.011$, $p < 0.0001$).

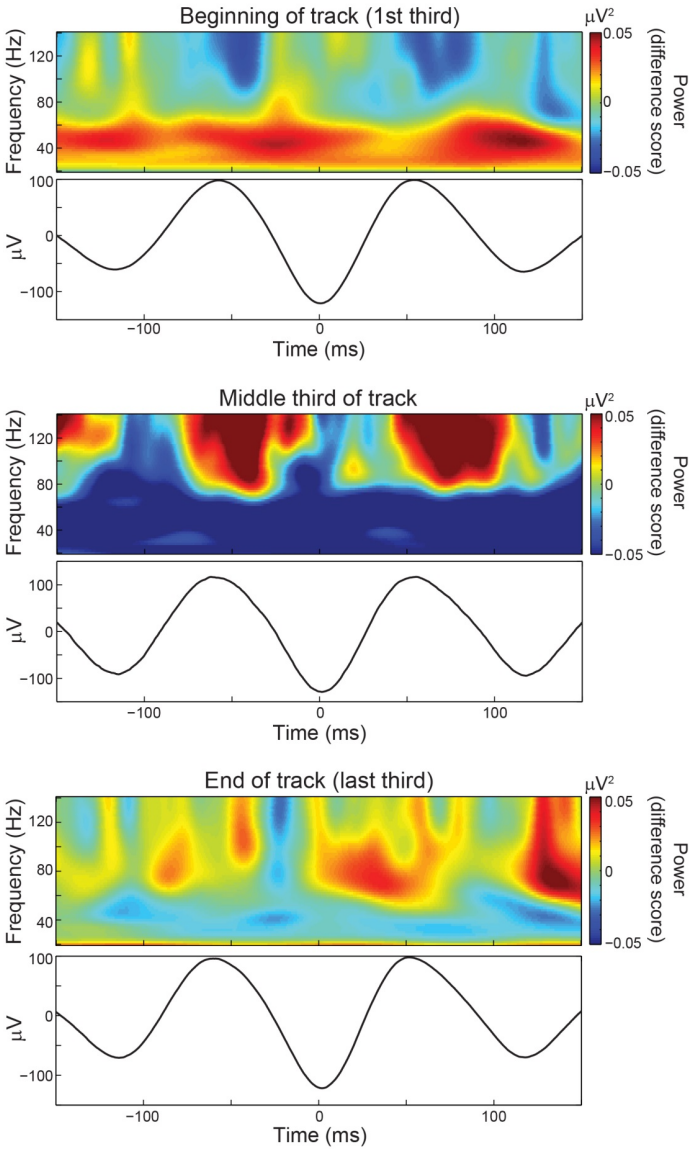

Figure S6, Related to Figure 8. Theta-locked spectral averages at different points of the trajectory. For the beginning (top panels), middle (middle panels), and end (bottom panels) of the linear track, color-coded power across time (x-axis) and frequencies (y-axis) is shown above corresponding averaged theta cycles (averaged across all recordings in all animals). Power is shown as a difference score (i.e., average power across the whole track was subtracted from power for each third of the track). Slow and fast gamma both phase-lock to theta but tend to occur at different theta

phases, as reported previously (Colgin et al., 2009). Note how slow and fast gamma are stronger at the start and end of the track, respectively, consistent with results shown in Figure 8B. Power observed in the middle third of the track peaks at frequencies >100 Hz, extends above 140 Hz, and likely reflects neuronal spiking (Belluscio et al., 2012).

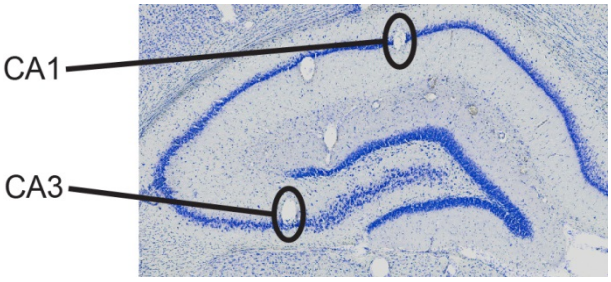

Figure S7, Related to Figure 6. Representative histological sections show recording sites in CA3 and CA1. Coronal sections stained with cresyl violet show typical tetrode tracks terminating in CA3 and CA1 cell body layers.

SUPPLEMENTAL EXPERIMENTAL PROCEDURES

Tetrode and recording drive preparation. Recording drives contained 13-14 independently movable tetrodes (13 in one rat, 14 in 4 rats). Tetrodes were constructed from 17 μm polyimide-coated platinum-iridium (90%-10%) wire (California Fine Wire). Electrode tips in tetrodes targeted toward cell body layers were plated with platinum to reduce single channel impedances to ~150-300 kΩ at 1 kHz.

Surgical implantation and tetrode placement. Recording drives were implanted above the right hippocampus (in mm: AP 3.8, ML 3.0, DV 1) on the day of surgery. Bone screws were placed in the skull, and the screws and the base of the drive were covered with dental cement to affix the drive to the skull. Two screws in the skull were connected to the recording drive ground.

Data acquisition. Experiments began when spikes emerged approximately at the proper depth for the region of interest (~2 mm for CA1 and ~3 mm for CA3) with amplitudes exceeding ~5 times the noise levels. Robust theta rhythms and sharp wave-ripple activity helped to verify that tetrodes were in the CA1 cell body layer.

The recording drive was connected to a multichannel, unity gain headstage (HS-54, Neuralynx, Bozeman, MT, USA). The output of the headstage was conducted via two lightweight tether cables through a multichannel slip-ring commutator to a data acquisition system that processed the signals through individual 24 bit AD converters (Digital Lynx, Neuralynx, Bozeman, MT, USA). Unit activity was bandpass filtered from 600 to 6000 Hz. Spike waveforms above a threshold set by the experimenter (~55-75 μV) were time-stamped and recorded at 32 kHz for 1 ms. Light-emitting diodes (LEDs)

on the headstage were used to track the animal's movements at a 30 Hz sampling rate. Additionally, video files were collected during every recording session.

LFPs (1 per tetrode) were recorded continuously in the 0.1-500 Hz band at a sampling rate of 2000 Hz. Notch filters were not used. Continuously sampled LFPs were recorded differentially against a common reference electrode placed in an electrically silent region (see Experimental Procedures). The common reference signal was duplicated using a breakout board (MDR-50 breakout board, Neuralynx, Bozeman, MT, USA) and recorded continuously against ground.

Testing procedures. After recovering from surgery, rats were trained to run three 10-minute sessions per day on a linear track. The linear track was 2 m long, 10 cm wide, and placed 64 cm above the floor. Rats were trained to run back and forth on the track, receiving small pieces of sweetened cereal or vanilla cookies on the ends. Every rat was trained on the linear track for at least 3 days prior to the start of recording. Between recording sessions, rats rested for ~10 minutes in a towel-lined, elevated flower pot.

Results, statistics, and data analyses. Results are reported as means ± SD and depicted in figures as means ± SEM, unless indicated otherwise. The results of all statistical tests are reported in the Results section. Reported t-tests are 2-tailed. Data were analyzed using custom software written in MATLAB (MathWorks, Natick, MA), unless indicated otherwise. Specific analysis methods are described in detail below and in the Experimental Procedures in the main text.

Spike sorting and cell classification. Spike sorting was performed offline using graphical cluster-cutting software (MClust; A.D. Redish, University of Minnesota, Minneapolis). Spikes were clustered manually in two-dimensional projections of the multidimensional parameter space (consisting of waveform amplitudes, energies, and peak-to-valley ratios). Autocorrelation and cross-correlation functions were additionally used to identify single units. Putative place cells were distinguished from putative interneurons on the basis of spike width, average firing rate, and bursting properties (Fox and Ranck, 1981; Henze et al., 2000; Harris et al., 2000; Frank et al., 2001). Firing rate maps (see below) were also used to identify putative place cells.

Place fields. Position was tracked using red and green LEDs on the rat's headstage. Spatial firing rate distributions ("place fields") for each well-isolated putative pyramidal cell were constructed in the standard manner by summing the total number of spikes that occurred in a given location bin (5 cm), dividing by the amount of time that the animal spent in that bin, and smoothing with a 25 cm (5 bins) SD Gaussian centered on each bin.

Place field acceptance criteria for single unit analyses. Individual place fields were required to have at least 3 contiguous bins with a firing rate above the lower of either 1 Hz or 10% of the peak firing rate of the cell. Additionally, the average firing rate across the rate map had to exceed 2.5 Hz. In order to exclude incomplete place fields, the start and stop bins were required to fall at least 15 cm away from the ends of the track for the field to be included in subsequent place field analyses. To account for trailing place field tails, the boundaries of the defined place fields were expanded in both directions until the minimum firing rate criterion (i.e., 1 Hz or 10% of the peak firing rate,

whichever was lower) was exceeded or the position was less than 15 cm from an end of the track. Within these expanded boundaries, place fields were defined according to the collection of bins that contained spikes, unless the firing rate rose above the minimum again before the 15 cm limits from the track end were reached. In this case, the last bin before the rise in rate occurred was counted as the place field boundary. Place fields for left and right running directions on the track were analyzed separately.

Gamma power estimation. Slow and fast gamma power were estimated using a wavelet transform method described previously (Tallon-Baudry et al., 1997). Signals were convolved by a family of complex Morlet's wavelets w(t, f), one for each frequency, as a function of time:

$$w(t, f) = A \exp(-t^2 / 2\sigma_t^2) \exp(2i\pi f t)$$

With $\sigma_f = 1/2\pi\sigma_t$. The coefficient A was set at:

$$(\sigma_t \sqrt{\pi})^{-1/2}$$

in order to normalize the wavelets such that their total energy was equal to 1. The family of wavelets was characterized by a constant ratio f/σ_f, which was set to 5.

Phase-locking of interneuron spikes to slow and fast gamma (Figure 2C). 201 interneurons recorded in or near the CA1 cell body layer were used for this analysis. For each interneuron, spikes that occurred during a traversal through a place field were selected and categorized as prospective if they occurred during a prospective traversal, retrospective if they occurred during a retrospective traversal, or ambiguous if they

occurred during an ambiguous traversal. The categories of traversals were defined as described in Experimental Procedures in the main text. Slow and fast gamma phases in CA1 at the time of spike occurrence were estimated using the LFP recorded from the same tetrode as the corresponding interneuron. Slow and fast gamma phases were estimated by first bandpass filtering the LFP in the slow and fast gamma frequency ranges, respectively. Then, a Morlet wavelet transform was performed on each filtered signal in order to extract the slow and fast gamma phase components corresponding to each spike time. The mean circular vector lengths of the slow and fast gamma phase distributions for each interneuron were then determined.

Place fields during periods of slow and fast gamma (Figures 3 and S3). Spikes that occurred during slow and fast gamma episodes were selected and binned across position within their respective place fields. The center of mass for the overall place field, and the slow and fast gamma downsampled place fields, was calculated in the following manner. For each bin in the place field, the product of the spike count and the position was calculated. These products were added together and divided by the sum of all of the spike counts to obtain the center of mass measure.

Position tracking using video files (Figure S1A). The video file for each linear track session was decomposed into red, green and blue frames (corresponding to light from red, green, and blue LEDs on the headstage). The blue frames were discarded because video camera settings were optimized to record red and green lights lining the front and back of the headstage, respectively. For each red and green frame, a convex hull was computed around any pixels breaking the intensity threshold. The center of mass (COM) of each hull provided the x-y location for each color. The animal's x-y

position was estimated from the average of the red and green convex hull COMs. The error between this computed x-y position and the x-y position acquired from the tracking data (i.e., the x-y position used in the place cell analyses) was minimized by adjusting the frame offset. This was done by sliding the two position vectors across each other in time and taking the mean of their squared differences. The offset with the lowest total mean was used. Finally, to find the area of the headstage, a convex hull was computed around the red and green pixels, and the inside area was computed. The maximal area (~40 cm^2) corresponds to the dimensions of the headstage plus a negligible amount of glare, and generally decreases when the animal looks up or down (due to tilting). Area was used because it offers a straightforward way of detecting tracking errors due to head tilting, obstruction of LEDs, or distortion from the camera angle. If the animals' position was consistently skewed by some sort of tracking error during prospective or retrospective coding, it should be evident as a systematic change in headstage area during the affected coding type.

Estimating running speed (Figure S4B). The running speed for each position (x_n) was estimated by taking the difference of the preceding position (x_{n-1}) and the following position (x_{n+1}) and dividing by the elapsed time (2*1/position sampling frequency). The temporal resolution of the speed was therefore 1/15 seconds because the position sampling frequency was 30 Hz.

Histology (Figure S7). For verification of tetrode locations, brains were cut coronally at 30 μm and stained with cresyl violet. Each section through the relevant part of the hippocampus was collected. All tetrode locations were identified, and the tip of each tetrode was localized by comparison across adjacent sections.

SUPPLEMENTAL REFERENCES

Fox, S. E., and Ranck, J. B., Jr. (1981). Electrophysiological characteristics of hippocampal complex-spike cells and theta cells. Exp. Brain Res. *41*, 399-410.

Frank, L. M., Brown, E. N., and Wilson, M. A. (2001). A comparison of the firing properties of putative excitatory and inhibitory neurons from CA1 and the entorhinal cortex. J. Neurophysiol. *86*, 2029-2040.

Harris, K. D., Henze, D. A., Csicsvari, J., Hirase, H., and Buzsaki, G. (2000). Accuracy of tetrode spike separation as determined by simultaneous intracellular and extracellular measurements. J. Neurophysiol. *84*, 401-414.

Henze, D.A., Borhegyi, Z., Csicsvari, J., Mamiya, A., Harris, K.D., and Buzsaki, G. (2000). Intracellular features predicted by extracellular recordings in the hippocampus in vivo. J. Neurophysiol. *84*, 390-400.

Tallon-Baudry, C., Bertrand, O., Delpuech, C., and Permier, J. (1997). Oscillatory gamma-band (30-70 Hz) activity induced by a visual search task in humans. J. Neurosci. *17*, 722-734.